Journal of Power Sources 195 (2010) 7338–7348

Contents lists available at ScienceDirect

Journal of Power Sources

journal homepage: www.elsevier.com/locate/jpowsour

Development and performance analysis of a metallic micro-direct methanol fuel cell for high-performance applications

Bo Zhang[a], Yufeng Zhang[a,b,*], Hong He[a], Jianmin Li[a], Zhenyu Yuan[a], Chaoran Na[a], Xiaowei Liu[a,b]

[a] MEMS Center, Harbin Institute of Technology, Harbin 150001, China
[b] Key Laboratory of Micro-Systems and Micro-structures Manufacturing, Ministry of Education, Harbin 150001, China

ARTICLE INFO

Article history:
Received 23 April 2010
Accepted 4 May 2010
Available online 13 May 2010

Keywords:
Micro-power sources
Micro-direct methanol fuel cell (μDMFC)
Current collectors
Micro-stamping
Stainless steel mesh

ABSTRACT

As a promising candidate for conventional micro-power sources, the micro-direct methanol fuel cell (μDMFC) is currently attracting increased attention due to its various advantages and prospective suitability for portable applications. This paper reports the design, fabrication and analysis of a high-performance μDMFC with two metal current collectors. Employing micro-stamping technology, the current collectors are fabricated on 300-μm-thick stainless steel plates. The flow fields for both cathode and anode are uniform in shape and size. Two sheets of stainless steel mesh are added between the membrane electrode assembly (MEA) and current collectors in order to improve cell performance. To avoid electrochemical corrosion, titanium nitride (TiN) layers with thickness of 500 nm are deposited onto the surface of current collectors and stainless steel mesh. The performance of this metallic μDMFC is thoroughly studied by both simulation and experimental methods. The results show that all the parameters investigated, including current collector material, stainless steel mesh, anode feeding mode, methanol concentration, anode flow rate, and operating temperature have significant effects on cell performance. Moreover, the results show that under optimal operating conditions, the metallic μDMFC exhibits promising performance, yielding a maximum power density of 65.66 mW cm^{-2} at 40 °C and 115.0 mW cm^{-2} at 80 °C.

Crown Copyright © 2010 Published by Elsevier B.V. All rights reserved.

1. Introduction

The rapid growth of portable electronics for both military and civilian applications over the past few decades has greatly accelerated the development of micro-power source technology, which is considered to be a crucial factor in the evolution of more advanced devices [1]. With respect to conventional large-sized power sources, micro-power sources can be described as lightweight, microfabricated power supply units of miniature dimensions, including micro-solar cells, micro-generators, micro-nuclear batteries, micro-fuel cells, etc. As a type of micro-fuel cell, the micro-direct methanol fuel cell (μDMFC) provides power by converting the energy of chemical reactants (methanol and oxygen) into electrical energy, it possesses significant advantages in terms of energy density, duration time, operating temperature, fuel storage, miniaturization and integration, and environmental issues [1,2]. Manufacturers in many countries (Ultracell, MTI Micro, Toshiba, Hitachi, Fujitsu, Samsung and Antig, among others) have realized the promising application of μDMFCs and have developed some prototypes [3].

Structurally, a μDMFC consists of two current collectors (anode and cathode) with flow fields, and a membrane electrode assembly (MEA) between them. The current collector is a vital component of the μDMFC [4], which not only supplies a passage for the transport of reactants, but also provides the structural support for the weak MEA and collects current. The current collector material must possess high electronic conductivity, good chemical stability, high thermal conductivity, high-mechanical strength for assembly, and compatible with simple and low-cost fabrication methods [5,6]. At present, three kinds of materials, silicon, metal, and polymer, are being investigated for use as current collectors in μDMFC [7,8]. Silicon is the most commonly used material because its microfabrication methods are relatively mature and well mastered. Lu et al. [9] developed a silicon-based μDMFC with an active area of 1.625 cm^2, yielding a maximum power density of 50 mW cm^{-2} at 60 °C. Its current collectors were microfabricated on silicon wafers using microelectromechanical system (MEMS) technology, and a layer of Cr/Cu/Au (0.01/3/0.5 μm) was deposited on the front of each wafer to reduce the contact resistance. Cao et al. [10] reported two μDMFC stacks consisting of six individual silicon-based cells with two different anode flow fields. The experimental results showed that the stack with double serpentine-type flow fields

* Corresponding author at: MEMS Center, Harbin Institute of Technology, Box 328, Harbin 150001, China. Tel.: +86 451 86413451; fax: +86 451 86413441.
E-mail address: edchang@126.com (Y. Zhang).

0378-7753/$ – see front matter. Crown Copyright © 2010 Published by Elsevier B.V. All rights reserved.
doi:10.1016/j.jpowsour.2010.05.011

Nomenclature

c_p	heat capacity (J mol^{-1} K^{-1})
C	molar concentration (mol m^{-3})
D	diffusivity (m^2 s^{-1})
E_{cell}	thermodynamic equilibrium potential (V)
F	Faraday's constant (C mol^{-1})
$\boldsymbol{F}_{st}$	surface tension force (N)
g	acceleration of gravity (m s^{-2})
G	Gibbs free energy (J mol^{-1})
H	enthalpy (J mol^{-1})
i	current density (A m^{-2})
$\boldsymbol{I}$	identity matrix
k_r	relative permeability
K	permeability
n	electro-osmotic drag coefficient
$\boldsymbol{n}_l$	interface normal
N	molar flux (mol m^{-2} s^{-1})
p	pressure (Pa)
q	heat generation rate (W m^{-2})
Q	heat source term
R	gas constant (mol m^{-3} s^{-1})
$R_{contact}$	contact resistance (Ω m^2)
S	mass source term
t	time (s)
T	operating temperature (K)
T_0	ambient temperature (K)
u	velocity (m s^{-1})
V_{cell}	cell voltage (V)

Greek letters

α	charge transfer coefficient
δ	thickness of the membrane (m)
η_a	anode overpotential (V)
η_c	cathode overpotential (V)
κ	ionic conductivity of membrane (Ω m^{-1})
ρ	density (kg m^{-3})
ϕ	volume fraction
σ	surface tension coefficient
θ	contact angle
τ	Dirac delta function
μ	dynamic viscosity (N s m^{-2})

Superscripts and subscripts

a	anode
acl	anode catalyst layer
c	cathode
ccl	cathode catalyst layer
$cross$	crossover
CO_2	carbon dioxide
i	methanol or oxygen
j	gas or liquid
m	methanol
mem	membrane
O_2	oxygen
ref	reference value

generated better performance, with the maximum output power reaching 151 mW at a voltage of 1.5 V. Compared to silicon current collectors, metal current collectors are cheaper and less prone to breakage during the assembling process. The existent problem is the electrochemical corrosion of metals. Milling, wire-cutting, etching and electroforming are commonly used in the microfabrication of metal current collectors. Lu and Wang [11] fabricated

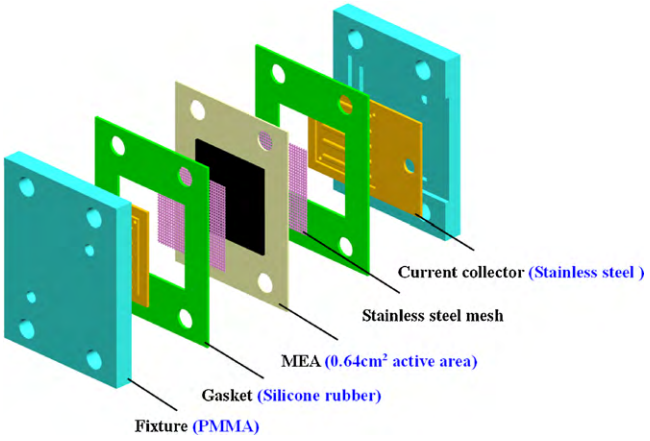

Fig. 1. Schematic of the metallic μDMFC.

a μDMFC of thin stainless steel plates using the photochemical etching method. To prevent corrosion, a gold layer with thickness of 0.5 μm was deposited on the surface of each stainless steel plate. Chan et al. [12] developed a metallic 6-cell μDMFC stack with passive operation, which provided 350 mW with 4.0 M methanol solution. The current collectors with a plurality of hexagonal holes were machined on 1.0-mm-thick stainless steel plates. The rise of polymer-based μDMFCs began with the development of some polymer materials, including polymethyl methacrylate (PMMA), polydimethylsiloxane (PDMS), SU8 and photosensitive glass. Hashim et al. [13] designed and fabricated a passive PMMA-based μDMFC stack with novel cathode structure. The maximum output power of this stack was about 12.05 mW. Ito and Kunimatsu [14] developed a novel, highly integrated μDMFC stack on a photosensitive glass substrate that featured an array of micro-holes for insertion of the MEAs. However, its maximum power output was only 1.04 nW.

In this paper, a high-performance metallic μDMFC was designed and fabricated. Following the construction of this μDMFC, we thoroughly investigated its performance under various parameters. Several suggestions are offered for optimization of the configuration and operating parameters of the μDMFC system for future development.

2. Experimental

The configuration of the metallic μDMFC is shown in Fig. 1. It consists of an MEA, two sheets of stainless steel mesh, two silicone rubber gaskets, two stainless steel current collectors, and two PMMA fixtures.

In this μDMFC design, both the anode and cathode current collectors have the same configuration. In order to enhance electronic conductivity and mechanical strength, the current collectors were fabricated on stainless steel plates with thickness of 300 μm by micro-stamping technology, a batch-fabricated, highly effective, easily operated, and low-cost method for machining metal parts. To enhance the stamped depth, the fabrication process was performed under warm hydro-mechanical conditions (90 °C) with methyl-silicone oil as the hydro-medium, in respect that this method effectively increases the limited drawing ratio of stainless steel [15]. Fig. 2 gives the micrograph of the microfabricated flow field with channels of 1000 μm width and 370 μm depth. It is worth mentioning that the cross-section of each channel was a trapezoid with an angle of 100 ± 1° that was shaped by the stamping process. Fig. 3(a) shows the SEM image of the surface of the stamped channel. It can be seen that some cracks were present after the fabrication process. To cover them, a 500-nm-thick TiN layer was deposited onto the

Table 1
Comparison of the five types of stainless steel mesh (0.8 cm × 0.8 cm).

Characteristics	SSM-1	SSM-2	SSM-3	SSM-4	SSM-5
Thickness (μm)	120	200	230	250	310
Opening width (μm)	118	297	488	672	1030
Opening area (mm^2)	0.0139	0.088209	0.238144	0.451584	1.0609
Opening number	1521	324	144	81	36
Strand width (μm)	85	140	165	250	260
Open ratio (%)	33.09	44.65	53.58	57.15	59.68
Internal resistance ($\Omega\,cm^2$) at 40 °C	1.431	1.648	1.734	1.879	2.025

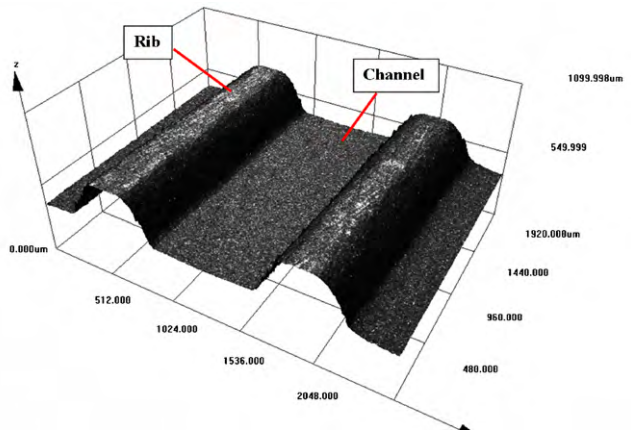

Fig. 2. Confocal laser scanning microscope (CLSM) image of the stamped channels of a metal current collector.

surface of each current collector using magnetron sputtering ion plating (MSIP) technology. Fig. 3(b) shows the surface of the channel following application of the TiN layer. This layer also protects the metal current collector from electrochemical corrosion.

The MEA (0.8 cm × 0.8 cm active area) was fabricated using the catalyst coated membrane (CCM) method. First, Nafion®117 membrane (Dupont™, 175 μm) was ion-exchanged to the Na^+ form by boiling in 0.5 M NaOH solution at 80 °C for 1 h and in deionized water at 80 °C for 1 h. The confected catalyst inks (consisting of Pt–Ru/Pt black, 5 wt.% solubilized Nafion®, isopropanol, alcohol, glycerol and deionized water) were uniformly sprayed onto polytetrafluoroethylene (PTFE) sheets through a spray gun, with catalyst loadings of 4.0 mg cm^{-2} (anode) and 2.0 mg cm^{-2} (cathode). The thin films were then transferred from the PTFE sheets to both sides of the membrane by hot pressing at 160 °C and 5 MPa for 90 s, forming the CCM. Afterwards, carbon papers (TGPH-090, Toray Inc.) were prepared with the hydrophobic (10 wt.% PTFE for anode, 30 wt.% PTFE for cathode) and pore-formed (NH_4HCO_3) treatment to form the gas diffusion layers (GDLs). Finally, the five-layered MEA was created with two GDLs hot-pressed on each side of the CCM at 130 °C and 4 MPa for 120 s. In order to improve cell performance, five different kinds of TiN-plated stainless steel mesh (represented by SSM-1 to 5) were employed between the MEA and current collectors. As shown in Table 1, each mesh contains square openings and strands of specified dimensions. PMMA with a heat-resistant treatment was used as the fixture material in this work. On one side of the PMMA fixture, a stepped groove was machined to provide a mount for current collector. Additionally, two circular holes were drilled on the other side as the ducts for reactants and products. The gasket material must have properties of good sealability, insulativity and compressibility. For this reason, two silicone rubber sheets were chosen as the anode and cathode gaskets with the same outline dimensions as the fixtures.

The disassembled components of the metallic μDMFC are shown in Fig. 4(a). Fig. 4(b) illustrates the schematic of the assembled μDMFC. To assemble the cell, the current collector was first embedded into the stepped groove of each fixture and pressed for about 4 h with the modified acrylate resin adhesive as a sealant and bonding agent between them. Second, metal tubes were inserted into the circular holes to form the inlet and outlet and fastened with the adhesive for no less than 24 h. To complete the assembly, two fixtures with current collectors and the other components were clamped together using four screws. The assembled μDMFC is shown in Fig. 4(c).

The metallic μDMFC was tested under atmospheric pressure. As illustrated in Fig. 5, four types of anode feeding modes were adopted for the fuel supply. Aqueous methanol solutions of different concentrations were fed to the cell anode at different flow rates by a peristaltic pump, while pure oxygen was supplied to the cathode

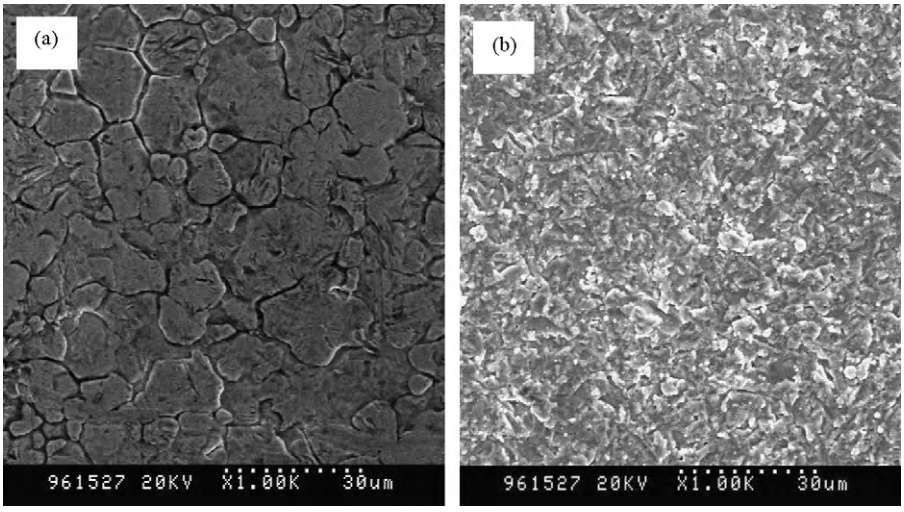

Fig. 3. SEM images of the surface of the channels: (a) without TiN layer; (b) with TiN layer.

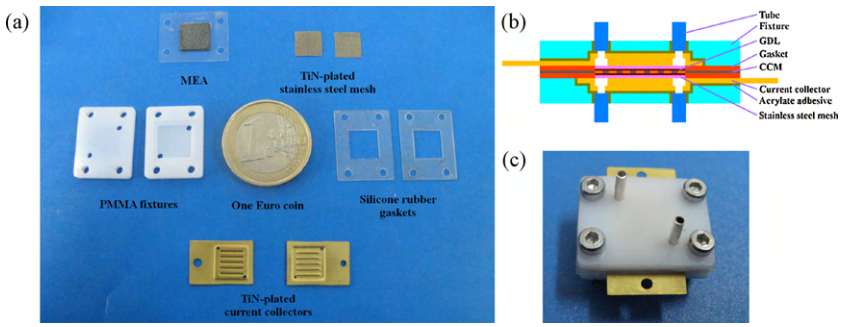

Fig. 4. The metallic μDMFC: (a) image of the disassembled components; (b) schematic of the assembly; (c) real features of the assembled μDMFC.

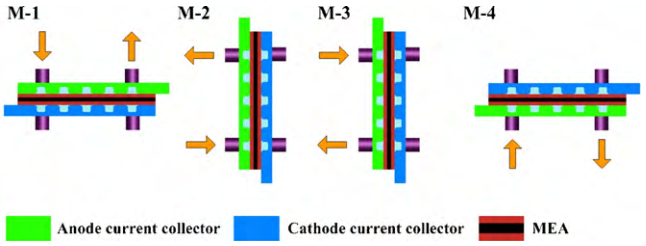

Fig. 5. Schematic of the four types of anode feeding modes.

at a constant gas flow rate of 50.0 ml min^{-1} by an oxygen cylinder. A programmable temperature test chamber was introduced to precisely regulate the cell temperature. The polarization curves and internal resistance of the cell were obtained on a DC electronic load (N3300A&N3302A, Agilent Technologies) and automatic rcl meter (PM6306, Fluke Co.), respectively.

3. Results and discussion

3.1. Basic performance

The basic performance of this metallic μDMFC was evaluated by both modeling and testing methods.

3.1.1. Model description

To better understand the basic performance of the μDMFC equipped with metal current collectors and stainless steel mesh, a two-dimensional mathematical model is developed. In this model, due to the parallel flow field and small size of the cell, variations along the flow channels are neglected. Hence, the *y*-direction of the model is chosen to be vertical to the flow direction of the channel, as diagrammed in Fig. 6. The simplifications and assumptions can be summarized as follows:

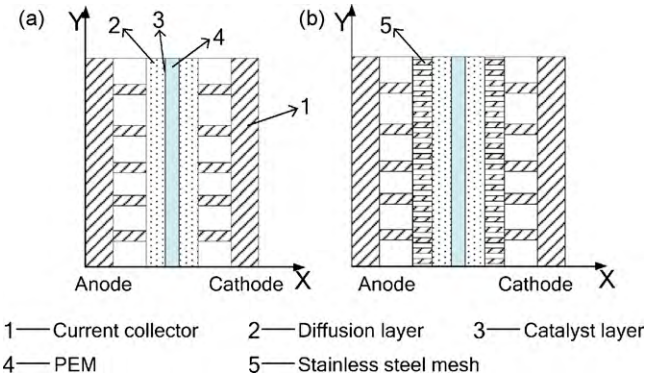

Fig. 6. Simulation domains of the model: (a) without mesh; (b) with mesh.

1. All processes in the μDMFC are under steady-state conditions.
2. The methanol concentration and velocity, as well as the liquid pressure, remain constant in the anode flow channel, as do the oxygen concentration, velocity, and gas pressure in the cathode flow channel.
3. In order to simplify the system, only single-phase flow is considered in the GDL, and the products, CO_2 and water, are neglected.
4. In the GDL and PEM, heat convection brought about by mass flow is ignored.
5. The catalyst layer is represented in a simplified manner as an interface between the GDL and PEM.

According to the mass conversation law, the mass transport of methanol and oxygen in GDLs can be formulated as

$$\nabla \cdot (-D_i^{eff} \nabla C_i + u_j C_i) = S_i \tag{1}$$

The GDL is modeled as a porous medium in which the diffusion coefficient of species *i* is modified by porosity. The volume average velocity of phase *j*, u_j, is calculated by a continuous function based on Darcy's law:

$$\nabla \cdot \left(\rho_j \left(-\frac{K k_{rj}}{\mu_j} \nabla p_j \right) \right) = S_j \tag{2}$$

According to the Tafel equation, the average current densities at the anode and cathode are expressed as [16]:

$$i_a = i_m^{ref} \frac{C_m}{C_m^{ref}} \exp\left(\frac{\alpha_a F}{RT} \eta_a \right) \tag{3}$$

$$i_c = i_{O_2}^{ref} \frac{C_{O_2}}{C_{O_2}^{ref}} \exp\left(\frac{-\alpha_c F}{RT} \eta_c \right) \tag{4}$$

The difference between i_a and i_c is the current density brought about by the methanol crossover from anode to cathode, which is driven by the electro-osmotic drag and concentration gradient. The flux of methanol through the PEM is therefore given as

$$N_{cross} = \frac{i_c - i_a}{6F} = -D_{m,mem} \nabla C_m + n_m \frac{i_a}{F} \tag{5}$$

Heat generated in the anode and cathode catalyst layers is defined as [16]:

$$q_{acl} = i_a \left(\eta_a - \frac{\Delta H_a - \Delta G_a}{6F} \right) \tag{6}$$

$$q_{ccl} = i_c \left(\eta_c - \frac{\Delta H_c - \Delta G_c}{4F} \right) - (i_c - i_a) \frac{\Delta H_a - \Delta G_a}{6F} \tag{7}$$

Heat loss caused by the mass flow in the flow channel is considered as

$$Q = \rho v c_p (T - T_0) \tag{8}$$

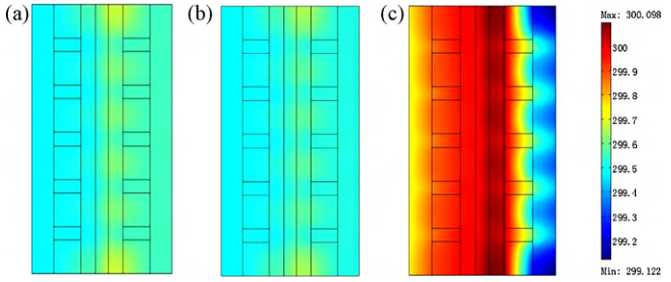

Fig. 7. Temperature distributions in μDMFCs with different current collector materials: (a) silicon; (b) stainless steel; (c) PMMA.

Cell voltage is estimated as follows:

$$V_{cell} = E_{cell} - \eta_a - \eta_c - i_a\frac{\delta}{\kappa} - i_a R_{contact} \quad (9)$$

The boundary conditions are generalized as follows. Heat flux boundaries are set at each side of the current collector surfaces to represent the transfer of heat between the μDMFC and the ambient environment; the surfaces of the sides of the current collectors are assigned two potential values for the equation of electron transport; all internal interfacial boundaries except the anode and cathode catalyst layers are set as continuous boundaries, resulting in the generation or consumption of each specie and heat; the remaining boundaries are set as insulating boundaries.

3.1.2. *Effect of the current collector material*

The influence of the current collector materials (i.e., silicon, stainless steel and PMMA) on cell performance was simulated using the case revealed in Fig. 6(a). The initial conditions were set as supplying 1.5 M methanol solution at 0.07 ml min^{-1} and 22 °C (295.15 K), which were identical to those used to test both the silicon-based μDMFC and the PMMA-based μDMFC in our previous work [17,18]. Fig. 7 shows the temperature distributions in μDMFCs with different current collector materials. Because of the excellent heat transfer qualities of silicon and stainless steel, uniform temperature distributions were achieved in their corresponding cells. Meanwhile, the temperature difference between anode and cathode was much larger in the PMMA-based cell. Thus, considering the necessity of heating or dissipating heat in cells under certain conditions, silicon and stainless steel appear to be more suitable as current collector materials.

By simulating this model, cell power densities with different current collector materials were obtained, as revealed in Fig. 8(a). It is obvious that the cell with stainless steel current collectors performed much better than the others. For the purpose of verifying the accuracy of simulation results, the metallic μDMFC (see Fig. 4(c)) was tested with the operating parameters remaining constant, and the testing results were compared to the data from our previous research [17,18]. As shown in Fig. 8(b), the metallic cell generated the highest power densities. This result demonstrates the superiority of stainless steel as the current collector material. Although the simulation and testing results were qualitatively similar, the magnitude of the simulation results was generally about two-thirds that of the testing results. This may be due to the simplifications and assumptions employed in our model and to deviations of some of the parameters used in the model from the actual values.

Compared to metal current collectors, the low electronic conductivity of silicon current collectors leads to a non-uniform current distribution, which is disadvantageous for reactant and catalyst utilization. In addition, the fragility of silicon leads to difficulties in compressing the cell for good packaging. Hence, the contact resistance in the cell is comparatively high. Although possessing low electronic conductivity and thermal conductivity, polymer is still a promising option for the current collector material by reason of its good chemical stability, light weight and low cost. For future applications, a feasible method might involve modifying the polymer material with some pretreatment to improve its characteristics.

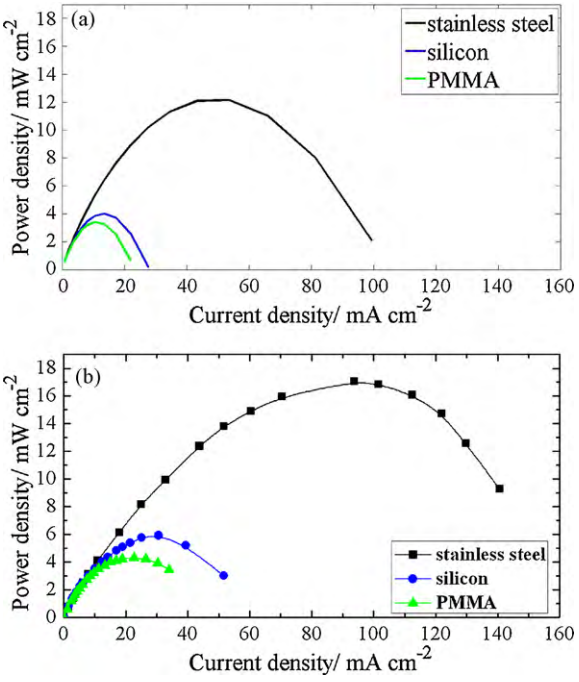

Fig. 8. Power density curves of the μDMFCs with different current collector materials: (a) simulation results; (b) testing results.

3.1.3. *Effect of the stainless steel mesh*

The cases in Fig. 6 were also simulated to estimate the effect of stainless steel mesh on cell performance. Initial conditions consisted of feeding 1.0 M methanol solution at 1.0 ml min^{-1} and at 40 °C (333.15 K). Fig. 9 shows the comparison of average methanol concentrations in the anode catalyst layers of μDMFCs with SSM-1 and without mesh. It is easy to see that SSM-1 augmented the resistance to methanol transport due to its mesh structure. According to Eq. (5), the lower methanol concentration in the anode catalyst layer results in less methanol permeating to cathode. It can be concluded that the stainless steel mesh has the function of inhibiting methanol crossover.

Fig. 10 presents both the simulation and testing results to determine the power density curves of μDMFCs with and without mesh. The experiments were conducted with 1.0 M methanol solution fed at 1.0 ml min^{-1} and at 40 °C. Both the simulation and testing

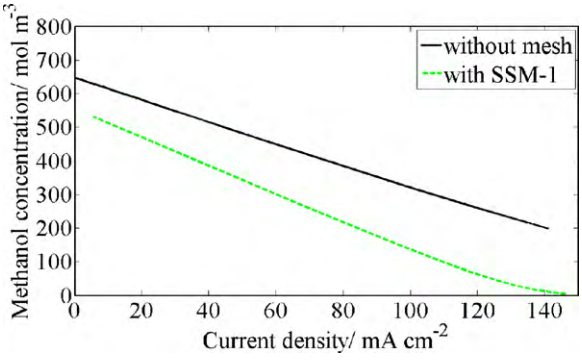

Fig. 9. Variations in average methanol concentrations in the anode catalyst layers with discharging current densities for the μDMFCs with SSM-1 and without mesh.

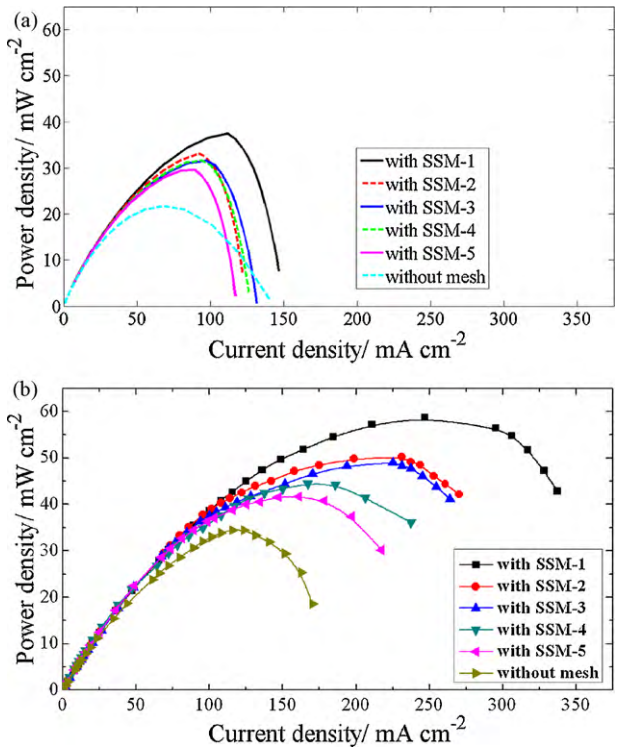

Fig. 10. Power density curves of the μDMFCs with and without the stainless steel mesh: (a) simulation results; (b) testing results.

results show that a cell equipped with any of the five types of mesh performed better than the equivalent cell without mesh. As in the case of cells with different types of collectors, the simulation results were about two-thirds of the testing results in magnitude. This phenomenon may occur for the same reasons as discussed above. In general, stainless steel mesh may have the following functions: (1) inhibiting methanol crossover; (2) reducing the internal resistance, as revealed in Table 1; (3) drawing CO_2 bubbles from the anode GDL and breaking them into smaller sizes via the mesh structure; (4) compressing GDLs more homogeneously to prevent deformation caused by the current collectors. Besides, Fig. 10 also shows that, compared with other types of mesh, the cell containing SSM-1 attained the highest power density of 58.76 mW cm^{-2}. This shows that the geometric parameters of stainless steel mesh significantly influence cell performance. On one hand, the lower the open ratio, the better the cell performance, by reason of the fact that a lower open ratio represents a larger contact area between mesh and GDL, which results in greater current-collecting ability. On the other hand, the smaller the opening area, the better the cell performance, by reason of the fact that smaller openings produce smaller CO_2 bubbles and smoother two-phase flow in the channels. Consequently, it is reasonable that SSM-1, which combines the lowest open ratio and the smallest opening area, should provide the best performance.

Fuel cell efficiency is another important index in evaluating μDMFC performance [19]. The Faraday efficiency (η), formulated in equation (10), is used to denote the fuel utilization rate, while the energy efficiency (ξ), formulated in Eq. (11), is used to indicate the rate of conversion of chemical energy into electrical energy. To further investigate the effect of stainless steel mesh, we performed a rough estimate [20] of the cell efficiencies with and without mesh. The cell was firstly fully filled with 1.0 M methanol solution by the peristaltic pump and operated at a fixed discharging current. After the cell had been stably running for 5 min, we shut down the pump and tested the transient cell voltage until it declined to zero. At this

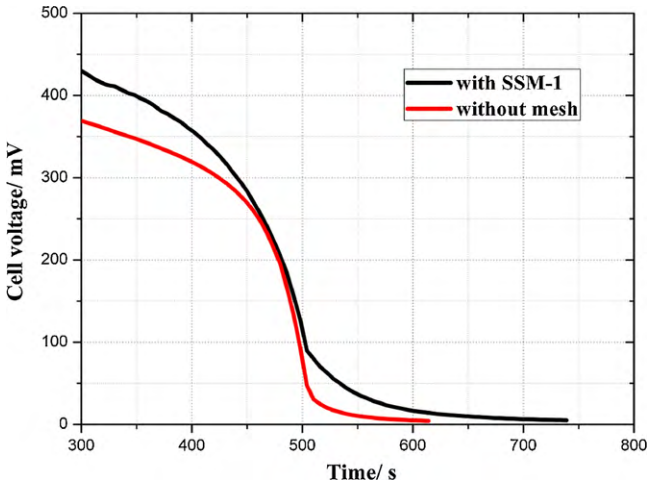

Fig. 11. Transient voltage curves of the μDMFCs with SSM-1 and without mesh when the fuel supplies were ceased.

point, all the methanol in the anode had been used up. The testing results are revealed in Fig. 11. Based on the parameters shown in Table 2, the cell efficiencies in the two cases were calculated according to Eqs. (10) and (11). It can be seen that the cell with SSM-1 gave a higher Faraday efficiency than the cell without mesh. As the volatilizing loss of methanol had no significant distinction in two cases, it was mainly because the mesh led to a reduction of the permeated methanol to cathode. Table 2 shows, furthermore, that the energy efficiency of the cell with SSM-1 was 30.3%, higher than that of the cell without mesh but also much lower than the Faraday efficiency. This reflects the fact that the chemical energy of the consumed reactants was converted largely into thermal energy, while only a small portion was converted into electrical energy. However, an energy efficiency of 30.3% is relatively high with respect to the levels currently being achieved with such devices, thus proving the advantage of stainless steel mesh in advancing the μDMFC for high power applications:

$$\eta = \frac{\text{discharging capacity } (C)}{\text{theoretical discharging capacity } (C)} \times 100\% = \frac{I_o t}{6 V_M C_M F} \quad (10)$$

$$\xi = \frac{\text{actual output energy (J)}}{\text{theoretical output energy (J)}} \times 100\% = \frac{I_o \int_0^t V(t)dt}{6 V_M C_M F E_0} \quad (11)$$

3.2. Effect of the anode feeding mode

Fig. 12 depicts the performance curves under different anode feeding modes, which were tested at 40 °C in the μDMFC with SSM-1, using 1.0 M methanol solution fed at 1.0 ml min^{-1}. As seen from this figure, the anode feeding mode greatly influences the cell performance. Based on former work [21] by Yang et al., we believe that this phenomenon is mainly due to the behavior of CO_2 gas bubbles in the anode flow field. To validate this deduction, we established a two-dimensional dynamic model to simulate the movement of a single CO_2 bubble in one straight channel of the parallel flow field. As shown in Fig. 13, the channel size is set at 1 mm × 8 mm, and the solution (fluid 2) flow rate is set at 0.045 m s^{-1}. Considering the aforementioned assumption that stainless steel mesh can break bubbles into smaller sizes, the diameter of the CO_2 bubble (fluid 1) is set at 0.6 mm and the initial position of the bubble is set at 2.0 mm from the inlet. In this model, by solving the volume fraction, we can trace the changes in the fluid movement trajectory of the gas–liquid interface. Hence, the movement state of the two-phase flow can be recorded. The model is developed based on the following assumptions:

Table 2
Parameters and results in Eqs. (10) and (11).

Parameter/result	Definition	Value	
		With SSM-1	Without mesh
I_0 (A)	Fixed discharging current	0.04	0.04
t (s)	Discharging time	439.2	314.7
V_M (L)	Methanol solution volume in the anode	3.4594×10^{-5}	3.2053×10^{-5}
C_M (mol l^{-1})	Initial methanol concentration	1.0	1.0
F (C mol^{-1})	Faraday constant	9.4685×10^4	9.4685×10^4
$V_{(t)}$ (V)	Transient voltage	Black curve in Fig. 11	Red curve in Fig. 11
E_0 (V)	Theoretical voltage	1.18	1.18
η (%)	Faraday efficiency	87.7	67.8
ξ (%)	Energy efficiency	30.3	19.7

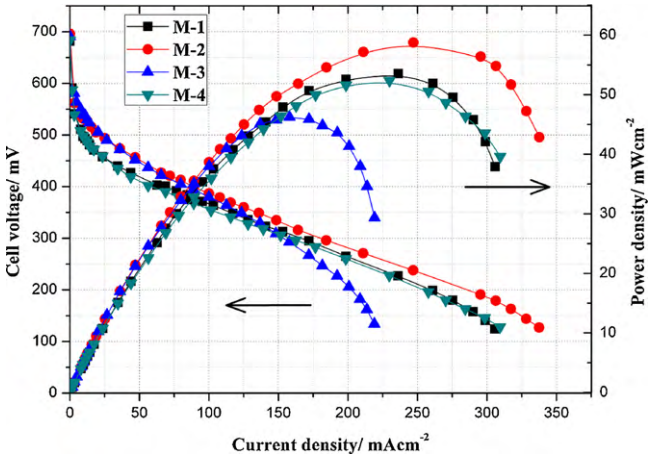

Fig. 12. Performance curves of the μDMFC with different anode feeding modes.

1. The two-phase mixture is considered to be an incompressible Newtonian fluid.
2. For each condition, pressure and temperature are constant.
3. Heat exchange and energy loss are neglected.
4. CO_2 gas bubble is directly released to the atmosphere, no reflux is engendered at the outlet.

In the straight channel, the bubble's motion is dominated mainly by four factors, buoyancy, gravity, viscous force and surface tension. According to the Navier–Stokes equation, the momentum transport equation for the CO_2 bubble is:

$$\rho\left(\frac{\partial \boldsymbol{u}}{\partial t} + \boldsymbol{u}\cdot\nabla\boldsymbol{u}\right) - \nabla\cdot(\mu(\nabla\boldsymbol{u} + \nabla\boldsymbol{u}^{\mathrm{T}})) + \nabla p = \boldsymbol{F}_{st} + \rho g \quad (12)$$

Here, the surface tension force, $\boldsymbol{F}_{st}$, is expressed as

$$\boldsymbol{F}_{st} = \nabla\cdot(\sigma(\boldsymbol{I} - (\boldsymbol{n}_l\boldsymbol{n}_l{}^{\mathrm{T}}))\tau) \quad (13)$$

The transport of the gas–liquid interface is given by

$$\frac{\partial\phi}{\partial t} + \nabla\cdot(\phi\boldsymbol{u}) + \gamma\left[\left(\nabla\cdot\left(\phi(1-\phi)\frac{\nabla\phi}{|\nabla\phi|}\right)\right) - \varepsilon\nabla\cdot\nabla\phi\right] = 0 \quad (14)$$

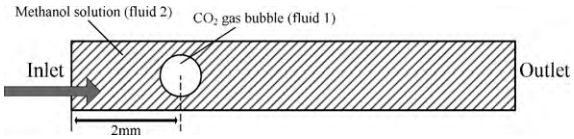

Fig. 13. Schematic of the 2D dynamic model when the CO_2 gas bubble is located at the initial position.

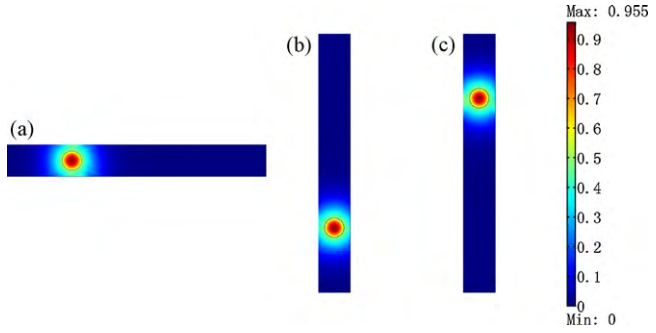

Fig. 14. Snapshots of the positions of the CO_2 gas bubbles for different feeding modes (t = 0 s): (a) M-1 or M-4; (b) M-2; (c) M-3.

The application mode uses the level set function to smooth the density and viscosity jump across the interface by letting:

$$\rho = \rho_{CO_2} + (\rho_m - \rho_{CO_2})\phi \quad (15)$$

$$\mu = \mu_{CO_2} + (\mu_m - \mu_{CO_2})\phi \quad (16)$$

The delta function is approximated by

$$\delta = 6\left|\phi(1-\phi)\right|\left|\nabla\phi\right| \quad (17)$$

And the interface normal is calculated from:

$$\boldsymbol{n}_l = \frac{\nabla\phi}{|\nabla\phi|} \quad (18)$$

In this model, only methanol solution enters through the inlet, and the pressure at the outlet is zero. All the walls have adopted the no-slip wall boundary.

Fig. 14 shows three initial positions of CO_2 bubbles for different feeding modes. Because the forces exerted on bubbles are basically consistent in M-1 and M-4, these two modes are simulated as one case, shown in Fig. 14(a). Fig. 15 shows the transient positions of the bubbles for different feeding modes at t = 0.1049 s. As can be

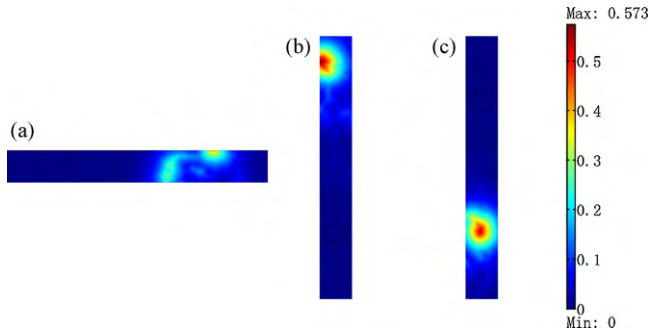

Fig. 15. Snapshots of the positions of the CO_2 gas bubbles for different feeding modes (t = 0.1049 s): (a) M-1 or M-4; (b) M-2; (c) M-3.

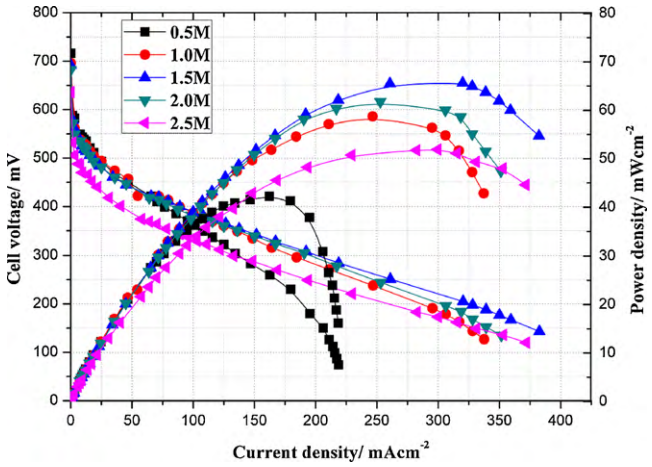

Fig. 16. Performance curves of the μDMFC with different methanol concentrations.

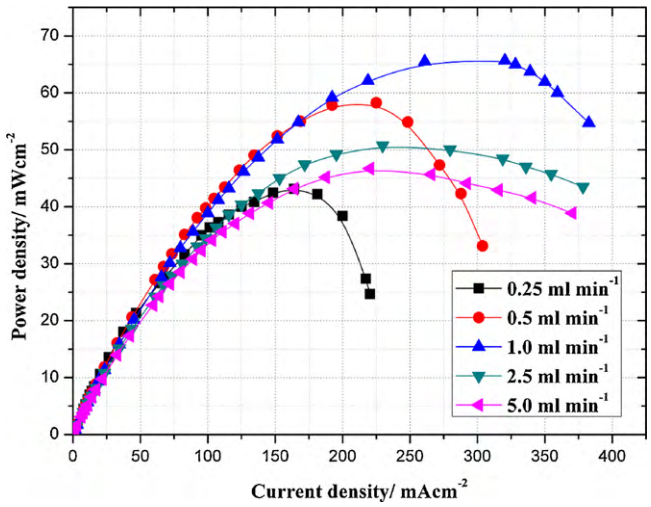

Fig. 17. Power density curves of the μDMFC with different anode flow rates.

seen, the position of the bubble in M-2 is closest to the outlet of the channel, proving that the rate of removal of the bubble is much higher with M-2 than with the other three modes. Moreover, ultimate simulation results showed that the complete removal time of bubbles with M-1 (M-4), M-2 and M-3 are 0.122467, 0.104941 and 0.134648 s, respectively. The removal time of CO_2 bubbles in different feeding modes correlates with the differences in cell performance revealed in Fig. 12, demonstrating that under otherwise identical operating parameters, the effect of the anode feeding mode is mainly engendered by the CO_2 bubbles behavior. Because portable applications require the μDMFC system to perform consistently in a variety of orientations, we suggest optimizing the system structure to ensure that each feeding mode has a consistent gas removal rate, thereby eliminating performance differences.

3.3. Effect of the methanol concentration

The influence of the methanol concentration on cell performance is shown in Fig. 16. Related experiments were carried out using mode M-2 with methanol solutions of five different concentrations (0.5, 1.0, 1.5, 2.0 and 2.5 M) fed at the same flow rate of 1.0 ml min^{-1} and at 40 °C, and with SSM-1. It can be seen that the best performance was found for a methanol concentration of 1.5 M and the maximum power density was 65.66 mW cm^{-2}, while the 0.5 M methanol solution gave the worst performance. The possible reasons are explained as follows. When a higher methanol concentration was utilized, excess methanol remained after the electrochemical reaction, inducing methanol crossover and generating an overpotential at cathode, which degraded the cell performance. On the contrary, a lower methanol concentration could not provide sufficient reactants to join the reaction, especially at high current densities. It is also noted that the optimal methanol concentration of 1.5 M validated in this work is higher than the concentration of around 1.0 M, which was more suitable for DMFCs with larger sizes [22,23]. This is mainly due to the fact that the methanol transport in micro-sized DMFCs is more difficult, so a higher methanol concentration is in demand.

3.4. Effect of the anode flow rate

To investigate the effect of the anode flow rate, the μDMFC equipped with SSM-1 was tested by using 1.5 M methanol solution at five different flow rates (0.25, 0.5, 1.0, 2.5 and 5.0 ml min^{-1}) and at 40 °C, and with mode M-2. The testing results are displayed in Fig. 17. As seen from this figure, when the flow rate increased from 0.25 to 1.0 ml min^{-1}, it is clear that the cell performance had a significant improvement accordingly. The reasonable explanations include two aspects. For one thing, an increment of the anode flow rate resulted in an increment of the methanol transport rate, which was effectual to overcome the mass transfer resistance induced by both the GDLs micro-porous structure and the reversed flow of CO_2 gas bubbles. For another, since the channels were narrow, CO_2 bubbles could easily occupy the anode flow field and disturb the liquid flow. As the anode flow rate increased, the removal rate of CO_2 bubbles would increase accordingly, leading to the decrement of the quantities and sizes of bubbles. These two aspects were both beneficial for the cell performance.

On the contrary, as shown in Fig. 17, when the anode flow rate continuously increased to 5.0 ml min^{-1}, the cell performance was found to deteriorate. In fact, as the key factors that determined cell performance, mass transport of methanol and removal of CO_2 gas bubbles were replaced by methanol crossover, mass transport of oxygen and heat loss when the μDMFC operated under higher anode flow rates. To methanol crossover, the permeating rate increased with the increment of the anode flow rate. Because the acceleration of the flow rate was ascribable to the enhancement of the static pressure which was brought by an external pump, this enhanced static pressure aggravated the methanol crossover. It is essential to note that when the static pressure became rather high, it could also provide a barrier of high resistance to the mass transport of oxygen in cathode. Moreover, because the reaction heat was released with the methanol solution, the rate of heat loss also increased with the anode flow rate, giving rise to a declination of the electrochemical kinetics. In a word, when the anode flow rate increased from 1.0 to 5.0 ml min^{-1}, the methanol crossover and heat loss were both impelled, while the mass transport of oxygen was restrained, thus the cell performance declined.

On the basis of the analysis above, we come to a conclusion that the effect of the anode flow rate is achieved by manipulating some factors that are crucial to cell performance, including mass transport of methanol and oxygen, removal of CO_2 gas bubbles, methanol crossover and heat loss. As a matter of fact, the leading factor that determines cell performance alternates with external loads, that is to say that the optimal anode flow rate is changeable at different current densities. Fig. 18(a) shows further polarization testing results by enhancing the current close to the limiting value. It can be seen that this figure is divided into five

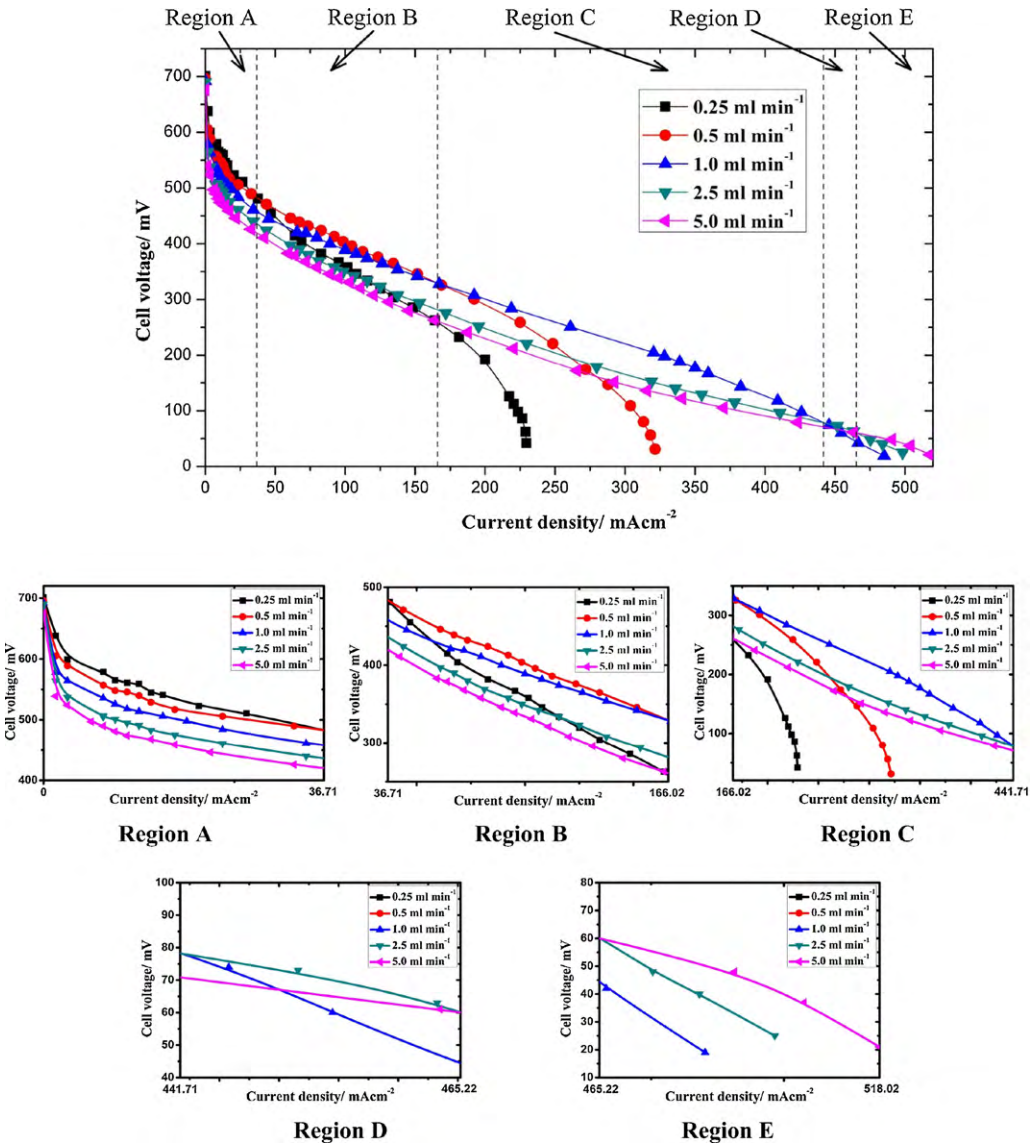

Fig. 18. Polarization curves of the μDMFC under different anode flow rates with the external load increasing from unloading to nearly zero: (a) image of the entire polarization performance with five different regions and (b) five enlarged images of the regions.

regions (represented by A–E), which are classified according to five current density intervals dominated by the five anode flow rates, respectively. Fig. 18(b) shows enlarged images of the five regions. As can be seen, although 1.0 ml min^{-1} gave the best performance in general, the flow rate that brought about the highest power density was not consistent in different regions. In region A (0–36.71 mA cm^{-2}), in respect that the methanol crossover was very serious and the required reactants, products and reaction heat were all of small amounts, 0.25 ml min^{-1}, which led to the lowest methanol permeating rate, performed the best. In region B (36.71–166.02 mA cm^{-2}) and region C (166.02–441.71 mA cm^{-2}), with the weakening of methanol crossover and the strengthening of other factors, 0.5 and 1.0 ml min^{-1} exhibited the best performance, respectively. When the current density increased to a high magnitude belonging to region D (441.71–465.22 mA cm^{-2}) or region E (465.22–518.02 mA cm^{-2}), the violent reaction brought about large amounts of consumed reactants, produced CO_2 gas and reaction heat, while little methanol permeated to cathode, and therefore, 2.5 and 5.0 ml min^{-1} were in the ascendant, respectively.

To satisfy various power requirements, we propose a novel "shifting-rate" feeding method to replace the conventional "constant-rate" feeding method. More specifically, according to Fig. 18, when the cell is working in one certain region, the flow rate will be shifted to the corresponding optimal magnitude. The dynamic performance of the μDMFC with "constant-rate" (1.0 ml min^{-1}) and "shifting-rate" feeding methods were compared in Fig. 19. The cell voltage was obtained by five current density steps, with every step persisting for 120 s, and the adopted current densities were selected from regions A to E, respectively. As can be seen from Fig. 19, the cell with the "shifting-rate" feeding method exhibited not a only better performance, but also a faster and more stable response. It is also worth mentioning that when the current density was kept at 476.56 mA cm^{-2}, a long period of stagnation was found with the "constant-rate" method. This behavior was mainly caused by the transient CO_2 bubbles blocking and the methanol starvation. Clearly, employing the "shifting-rate" feeding method can effectively improve cell performance, and this method can be easily achieved in practical operation. We can use a microprocessor to monitor the current output of the μDMFC, and then modulate the frequency of the feeding pump according to the current feedback. As a result, the anode flow rate can be controlled in real time.

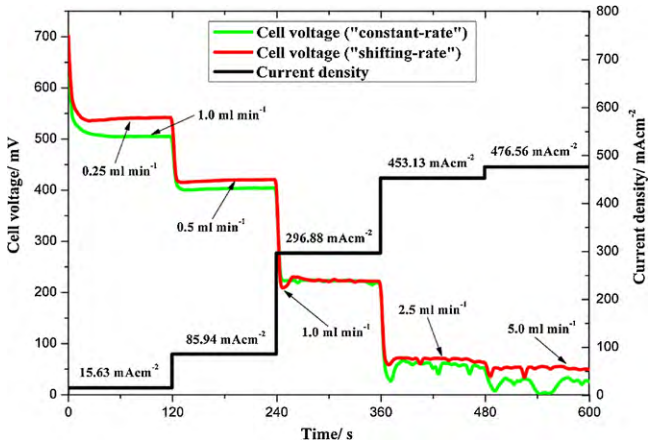

Fig. 19. Transient voltage curves of the μDMFC with the "constant-rate" and "shifting-rate" feeding methods under five current density steps.

3.5. Effect of the cell temperature

Controlling the operating temperature is critical to the improvement of μDMFC performance. It is commonly believed that an increase in the operating temperature can lead to a marked increment in cell performance. The probable benefits of increasing the temperature are (1) increased activity of the catalysts; (2) reduction in the PEM resistance; and (3) increased mass transport in the cell. However, in the course of our experiments, we found that the variation in cell performance with changes in the operating temperature was not uniform. The experiments were carried out under the aforementioned optimal operating conditions, and the adopted temperatures were 40, 60 and 80 °C. Fig. 20 shows the testing results. Based on our prior understanding of the benefits of raising the temperature, the cell performance was expected to be the best at 80 °C, but in fact, this was not so. As seen from Fig. 20, although 80 °C was in the ascendant when the current density was less than 260.92 mA cm^{-2}, once the current density exceeded this value, 60 °C gave better performance. It appeared likely to us that this unexpected temperature dependence was a consequence of the anode flow rates (1.0 ml min^{-1}) being insufficient to provide either an adequate methanol transport rate for the rapid reaction or an efficient removal rate of the large amounts of CO_2 bubbles generated at high current densities. To test this hypothesis, we increased the anode flow rate to 2.5 and 5.0 ml min^{-1} while keeping the other

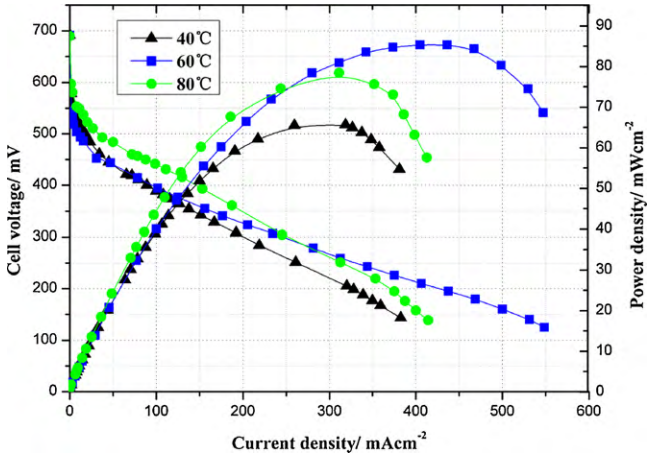

Fig. 20. Performance curves of the μDMFC at different operating temperatures with the anode flow rate of 1.0 ml min^{-1}.

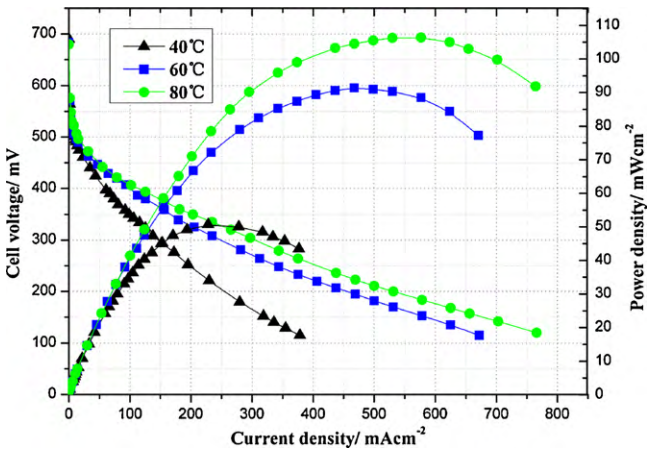

Fig. 21. Performance curves of the μDMFC at different operating temperatures with the anode flow rate of 2.5 ml min^{-1}.

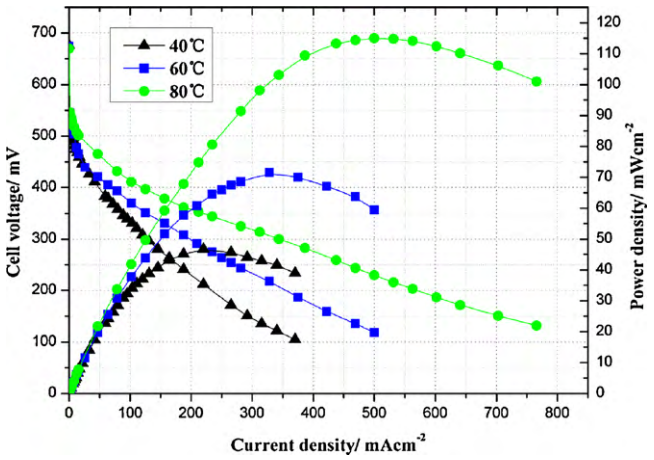

Fig. 22. Performance curves of the μDMFC at different operating temperatures with the anode flow rate of 5.0 ml min^{-1}.

operating conditions remaining constant. The testing results are revealed in Figs. 21 and 22. At a higher flow rate, the cell performance at 80 °C was much better than that at 40 or 60 °C. Moreover, the higher the flow rate, the larger the performance difference. This finding is consistent with our hypothesis. We thus conclude that in order to ensure the best cell performance at different operating temperatures, the anode flow rate must be regulated. This finding is meaningful with respect to future applications. In addition, it is worth noting that, as shown in Fig. 22, the maximum power density reached 115.0 mW cm^{-2} at 80 °C, a remarkable performance for μDMFCs.

4. Conclusions

This paper reports the development of a metallic μDMFC with an active area of 0.64 cm^2. By means of micro-stamping technology, current collectors with flow channels were fabricated on stainless steel plates with thickness of 300 μm under warm hydromechanical conditions at 90 °C. To enhance the cell performance, two sheets of stainless steel mesh were placed between the MEA and current collectors. The performance of this metallic μDMFC has been thoroughly studied under various operating parameters. Based on the simulation and testing results, the following conclusions can be drawn:

1. The metallic μDMFC exhibited better performance than the cells with silicon or PMMA current collectors, due to the excellent characteristics of stainless steel.
2. The inclusion of stainless steel mesh is helpful in improving cell performance and efficiency. The best performance was achieved with SSM-1, which possesses the lowest open ratio and smallest opening area. Further study is required to determine the influence of the opening shape and the feasibility of replacing traditional carbonic GDLs with the metal mesh.
3. Testing results show that the anode feeding mode has a significant effect on cell performance, and this effect may be caused by differences in the removal time of CO_2 gas bubbles. Further study is focused on finding a solution to eliminate these differences.
4. The optimal methanol concentration is 1.5 M, higher than the optimal concentration (approximately 1.0 M) for DMFCs of large sizes.
5. The effect of the anode flow rate on cell performance is somewhat complicated. Although the overall highest power density was achieved at 1.0 ml min^{-1}, the optimal anode flow rate for best performance was not consistent at different current densities. Based on the testing results, a novel "shifting-rate" feeding method was introduced to optimize the anode feeding mechanism and was shown to be feasible.
6. An increase in the operating temperature cannot directly bring about the improvement in cell performance unless accompanied by an increase in the anode flow rate. By controlling the anode flow rate, the maximum power density of this cell reached 65.66 mW cm^{-2} at 40 °C and 115.0 mW cm^{-2} at 80 °C. In general, the performance of this metallic μDMFC is promising for future applications.

Acknowledgements

The work described in this paper was supported by the National Natural Science Funds of China (No. 60806037), the National High Technology Research and Development Program ("863" Program) of China (No. 2006AA04Z353), the grant from the Ph.D. Programs Foundation of Ministry of Education of China (No. 20070213057), and the Natural Scientific Research Innovation Foundation in Harbin Institute of Technology (HIT. NSRIF. 2009008).

References

[1] C.K. Dyer, J. Power Sources 106 (2002) 31.
[2] Z.G. Shao, F.Y. Zhu, W.F. Li, et al., J. Power Sources 161 (2006) 813.
[3] http://www.fuelcelltoday.com.
[4] P. Qian, H.M. Zhang, J. Chen, et al., J. Power Sources 175 (2008) 613.
[5] X.G. Li, I. Sabir, Int. J. Hydrogen Energy 30 (2005) 359.
[6] A. Hermann, T. Chaudhuri, P. Spagnol, Int. J. Hydrogen Energy 30 (2005) 1297.
[7] T. Pichonat, B. Gauthier-Manuel, Microsyst. Technol. 13 (2007) 1671.
[8] X.W. Liu, B. Zhang, Y.F. Zhang, et al., Progress Chem. 21 (9) (2009) 1980.
[9] G.Q. Lu, C.Y. Wang, T.J. Yen, et al., Electrochim. Acta 49 (2004) 821.
[10] J.Y. Cao, Z.Q. Zou, Q.H. Huang, et al., J. Power Sources 185 (2008) 433.
[11] G.Q. Lu, C.Y. Wang, J. Power Sources 144 (2005) 141.
[12] Y.H. Chan, T.S. Zhao, R. Chen, et al., J. Power Sources 178 (2008) 118.
[13] N. Hashim, S.K. Kamarudin, W.R.W. Daud, Int. J. Hydrogen Energy 34 (2009) 8263.
[14] T. Ito, M. Kunimatsu, Electrochem. Commun. 8 (2006) 91.
[15] Y.C. Xu, D.C. Kang, J. Harbin Inst. Technol. 35 (10) (2003) 1165.
[16] R. Chen, T.S. Zhao, W.W. Yang, et al., J. Power Sources 175 (2008) 276.
[17] X.C. Tang, Y.F. Zhang, B. Zhang, et al., Nanotechnol. Precis. Eng. 7 (1) (2009) 76.
[18] Y.F. Zhang, P. Zhang, B. Zhang, et al., J. Funct. Mater. Devices 14 (2) (2008) 408.
[19] J.G. Liu, T.S. Zhao, R. Chen, et al., Electrochem. Commun. 7 (2005) 288.
[20] Y.Q. Jiang, X.H. Wang, L.Y. Zhong, et al., J. Micromech. Microeng. 16 (2006) S233.
[21] H. Yang, T.S. Zhao, Q. Ye, J. Power Sources 175 (2005) 276.
[22] A.A. Kulikovsky, Electrochem. Commun. 4 (2002) 939.
[23] K. Scott, W. Taama, J. Cruickshank, J. Appl. Electrochem. 28 (1998) 289–297.